Angewandte Chemie
Eine Zeitschrift der Gesellschaft Deutscher Chemiker

Supporting Information

Comprehensive H_2O Molecules Regulation via Deep Eutectic Solvents for Ultra-Stable Zinc Metal Anode

M. Li, X. Wang, J. Hu, J. Zhu, C. Niu, H. Zhang, C. Li, B. Wu, C. Han*, L. Mai**

Experimental Section

Electrolyte configuration:

Pure aqueous electrolytes were prepared by dissolving 1M $Zn(TFSI)_2$ (bis(trifluoromethylsulfonimide zinc) or 1M $ZnSO_4$ salt in deionized water.1M $Zn(TFSI)_2$ (Zinc bis(trifluoromethylsulfonyl)imide salt) or 1 M $ZnSO_4$ was dissolved into deionized water as pure aqueous electrolytes. Hybrid electrolytes were prepared by dissolving 1M $Zn(TFSI)_2$ in hybrid solvents with reconstructed hydrogen bonds. The hybrid solvents were prepared by mixing sulfolane with deionized water. According to different proportions, the molar ratio of sulfolane and water molecule (sulfolane : H_2O) is 0.05:1, 0.2:1, 0.5:1, 1:1 and 2:1 respectively.

***Synthesis of $V_2O_5{\cdot}nH_2O$*:**

The $V_2O_5{\cdot}nH_2O$ (VOH) were prepared by a facile hydrothermal method.[1] Typically, 0.3 g V_2O_5 were dissolved in 30 mL of deionized water with 4 mL H_2O_2 added dropwise. Afterwards, the mixed solution was transferred into a 50 mL Teflon-lined autoclave and maintained at 200°C for 48 h. *VOH* was obtained after centrifuged several times with alcohol and dried at 70 °C in a vacuum oven for 12 h.

Electrolyte/Materials Characterization:

The crystal structures are evaluated by a Bruker D8 Advance X-ray diffractometer with Cu Kα radiation. The morphologies of samples are conducted using field emission scanning electron microscopy (FESEM; JEOL JSM-7100F, 20 kV) and Super-large depth of field 3D microscopic system (KEYENCE, VHX-600E). *In-situ* microscope images are obtained in real time by the combination of microscope and electrochemical workstation. Fourier-transform infrared (FTIR) spectra were recorded on a Nicolet Nexus 670 Fourier transform infrared spectrometer (FT-IR). *In-situ* ATR-FTIR measurements using a Thermo scientific iS50 spectrometer. The spectra were collected in external reflection using a liquid-N_2-cooled MCT (mercury−cadmium−telluride) detector. The single-beam spectra were acquired at 4 cm^{-1} spectral resolution with an interferometer frequency of 40 kHz and then Fourier transformed^{1}H NMR spectra were was performed on Bruker Avance III, 600 M. DSC curves were tested by American Ta Q2000 with a temperature ramp of 5 °C min^{-1}. 3D images of electrode surfaces are characterized by confocal laser microscopy (LSM 800). Electrolytes viscosity are measured by rotational viscosity test HAAKE MARS III (Thermofisher, USA). The X-ray absorption spectra (XAS) including X-ray absorption near-edge structure (XANES) and extended X-ray absorption fine structure (EXAFS) of the samples at Zn K-edge (9659 eV were collected at the Singapore Synchrotron Light Source (SSLS) center, where a pair of Chanel-cut Si (111) crystals was used in the monochromator. The Zn K-edge XANES data were recorded in a transmission mode. Zn foil and ZnO were used as references. The storage ring was working at the energy of 2.5 GeV with an average electron current of below 200 mA. The acquired EXAFS data were extracted and processed according to the standard procedures using the ATHENA module implemented in the FEFIT software packages. The k3-weighted Fourier transform (FT) of x(k) in R space was obtained over the range of 0-14.0 $Å^{-1}$ by applying a Besse window function.

Fabrication of symmetric/asymmetric battery:

For Zn//Zn symmetric battery, two pieces of polished Zn foils with a thickness of 100 μm (Φ10 mm) were used as two electrodes for symmetric cell. Different electrolytes (1 M $ZnSO_4$, 1 M $Zn(TFSI)_2$, 0.05:1, 0.2:1, 0.5:1, 1:1 and 2:1 hybrid electrolytes) were added into the CR2025-type coin cell with a piece of glass fiber (GF/D, Whatman) as a separator. For Zn//Ti or Zn//SS (stainless steel mesh) asymmetric battery, the same assembly process, the only difference being the replacement of one side of the Zn foil with a titanium (Ti) foil (32 μm, Φ10 mm) or stainless steel mesh.

Fabrication of Zn−VOH full battery:

The cathode was prepared by mixing the active materials (VOH), conductive carbon (Super P), and PVDF in a weight ratio of 7:2:1 in NMP. Next, the slurry was cast onto Ti foil and dried in vacuum oven at 60 °C for a night. The mass loading in the cathode is 1~2 mg cm^{-2}. The electrode was cut into round disks (Φ=10 mm) as the cathode. Zn foil (0.15 mm) was directly used as the anode after a polishing, and a pure aqueous or hybrid 1 M $Zn(TFSI)_2$ as the electrolyte, glass fiber (GF/D, Whatman) as the separator in CR2025 coin cells. For homemade modular cell, the Zn foil (0.02 mm) and cathode was cut into 3 cm × 3.5 cm and 4 cm × 4 cm with tab, respectively. The mass loading in the cathode is ~4 mg cm^{-2}. For pouch cell, the cathode was prepared by mixing the active materials (VOH), conductive carbon (Super P), and PTFE in a weight ratio of 7:2:1. The mixture was then rolled on Ti mesh and finally dried at 80 °C for 12 h. The Zn foil (0.1 mm) and cathode was cut into 5 cm × 9 cm with tab. The mass loading in the cathode is ~15 mg cm^{-2}.

Electrochemical Characterization:

The performances of Zn//Zn symmetric batteries Zn//Ti asymmetric batteries, and Zn−VOH full batteries were collected by battery test system (Neware BTS-4000). The homemade modular cell and pouch cell were tested on Neware battery test systerm (CT-4008-5V6A-S1-F, Shenzhen China). The linear scan voltammetry (LSV), Chromoamperograms (CAs) are carried out utilizing an electrochemical workstation (CHI 760E Chenhua,

Shanghai). The charge-discharge experiments are performed on a Land BT2000 battery test system (Wuhan, China) at low temperature (−20℃) by high &low temperature test chamber (KW-GD-80F, Dongguan Kowin Testing Equipment Co., LTD). The stainless steel (SS)/electrolytes-GF/SS cells were assembled to measure ionic conductivities and calculated according to the following equation: $\sigma=L/R_eS$ (L is the thickness, S is the contact area, R_e is the electrolyte resistance). The electrochemical impedance spectroscopy (EIS) was measured by using an Autolab PGSTAT302N in the frequency range from 10^6 to 10 Hz with a perturbation of 10 mV.

Molecular dynamics (MD) simulations:

All molecular dynamics (MD) simulations were performed with Gromacs, version 2019.6.[2] The simulation systems were constructed by uniformly adding 100 Zn^{2+}, 200 $TFSI^-$ into pure water (5500 molecules) or a mixture of 490 water molecules and 960 sulfolane molecules as follows, which was done by PACKMOL software.[3]

Electrolyte model	H_2O molecules	Sulfolane molecules	Zn^{2+}	$TFSI^-$
Pure aqueous electrolyte	5500	0	100	200
Hybrid electrolyte	480	960	100	200

The GAFF force field[4] was employed for $TFSI^-$ and sulfolane, while water was modelled by the SPC/E model[5]. For Zn^{2+}, the parameters by Li at al.[6] were used. The atomic charges of $TFSI^-$ and TMS were derived with the help of Multiwfn program by fitting to electrostatic potential of the molecular structure optimized at the B3LYP/def2TZVP level of theory in Gaussian 16.[7] Van der Waals interactions were represented by the Lennard Jones (LJ) potential with a cut-off value of 1.2 nm. The LJ interaction parameters between different atom pairs were derived from the Lorentz-Berthelot mixing rules. Short-range electrostatic interactions were truncated at 1.2 nm, while the long-range part was calculated with the particle-mesh Ewald method. Energy-minimization with steepest descent algorithm was conducted for initial configurations. Then 10-ns MD runs were carried out at 298.15 K and 1 bar with V-rescale thermostat and Berendsen barostat. The equations of motion were integrated by the leapfrog algorithm with a time step of 1 fs. Three-dimensional periodic boundary conditions were applied in all simulations.

Finite Element Analysis Method:

The electric field distribution and current density distribution were simulated and calculated by COMSOL software, and the two cases without coating (model 1) and with coating (model 2) were compared. The detailed parameters are as follows:

Parameter	Model 1	Model 2
Model size	12 μm · 9 μm	12 μm · 9 μm
Surface raised radius	1.0 μm	1.0 μm
Sulfolane adsorption layer	0	0.2 μm
Metal Zinc conductivity	1.67×10^7 S/m	1.67×10^7 S/m
Electrolyte conductivity	1.6 S/m	0.4 S/m
Sulfolane conductivity	No	2×10^{-8} S/m
Upper boundary potential	68 mV	115 mV
Lower boundary potential	0	0

Density functional theory (DFT) Calculations:

All density functional theory (DFT) calculations were accomplished using Vienna Ab initio simulation package (VASP) [8]. The generalized gradient approximation (GGA) functionals were considered by Perdew-Burke-Ernzerh as well as projector augmented wave method (PAW-PBE) to describe exchange-correlation

effects between electrons [9]. The hexagonal Zn (space group: P63/mmc, the lattice constants: a = b = 2.66 Å and c = 4.95 Å) is selected to obtain Zn (0001 and 1000) surface, a 4 × 4 supercell of Zn (0001 and 1000) surface is constructed as the corresponding adsorption model. The surface energy calculation for the stoichiometric slab is token as follows: $E_{surface}=\frac{E_{slab}-(N_{slab}/N_{bulk})E_{bulk}}{2A}$, where E_{slab} and E_{bulk} represent the total energies of relaxed slab and bulk nit cell, respectively. N_{slab} and N_{bulk} are the atom numbers of the slab and the bulk unit, respectively. Additionally, A represents the surface area of slab model.[10] The energy cutoff for plane-wave basis set was 500 eV, and a Monkhorst-Pack k-mesh of 3 × 3 × 1 was adopted. In the optimization process, the convergence criterion for the electronic self-consistent field (SCF) loop was set to 1×10-5 eV/atom. The atomic structures were optimized until the residual forces were below 0.05 $eVÅ^{-1}$. In addition, the energy barriers of Zn^{2+} transporting on Zn (0001) and Zn(0001)−Sulfolane surfaces were explored by the using Nudge Elastic Band (CI-NEB) method.[11] The quantum chemistry (QC) calculations were performed with the help of Gaussian package. The electrostatic potential results were predicted by the M06-2x functional with 6-311+g(2df,2p) basis set.

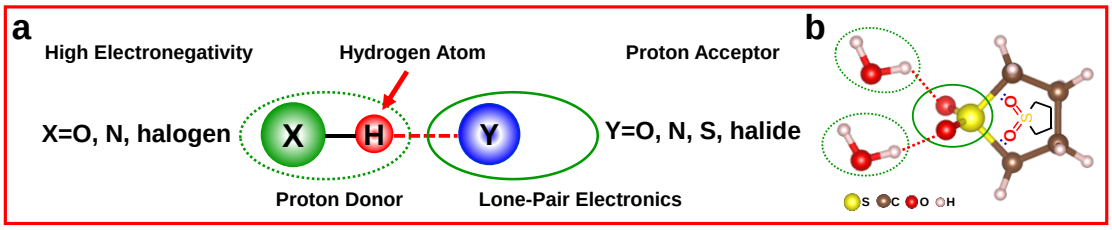

Figure S1. (a) Schematic diagram of typical hydrogen bond formation. (b) Schematic diagram of H_2O-sulfolane hydrogen bond.

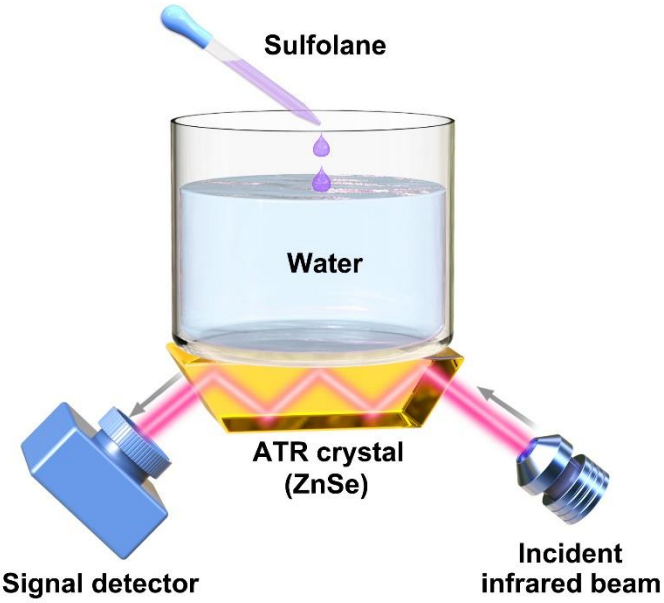

Figure S2. Schematic diagram of in-situ ATR-FTIR. Using the extremely low scattering losses of ZnSe crystals as refractors to reduce the weakening of the incident signal during reflection. Using pure deionized water as the base, sulfolane is added dropwise at a constant rate throughout the process until the final molar ratio of sulfolane to water is 2:1. The entire process is accompanied by thorough stirring to ensure that the sulfolane and water are mixed uniformly.

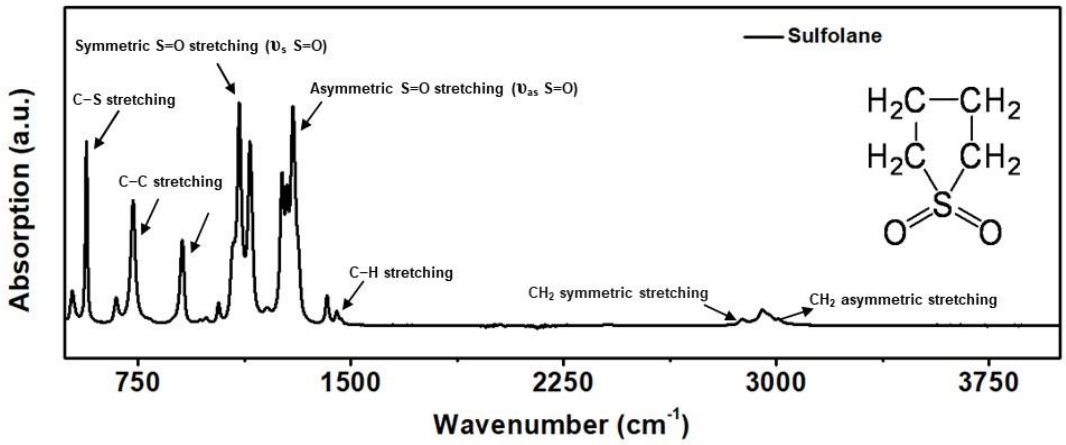

Figure S3. The FTIR spectrum of sulfolane and corresponding molecular structure.

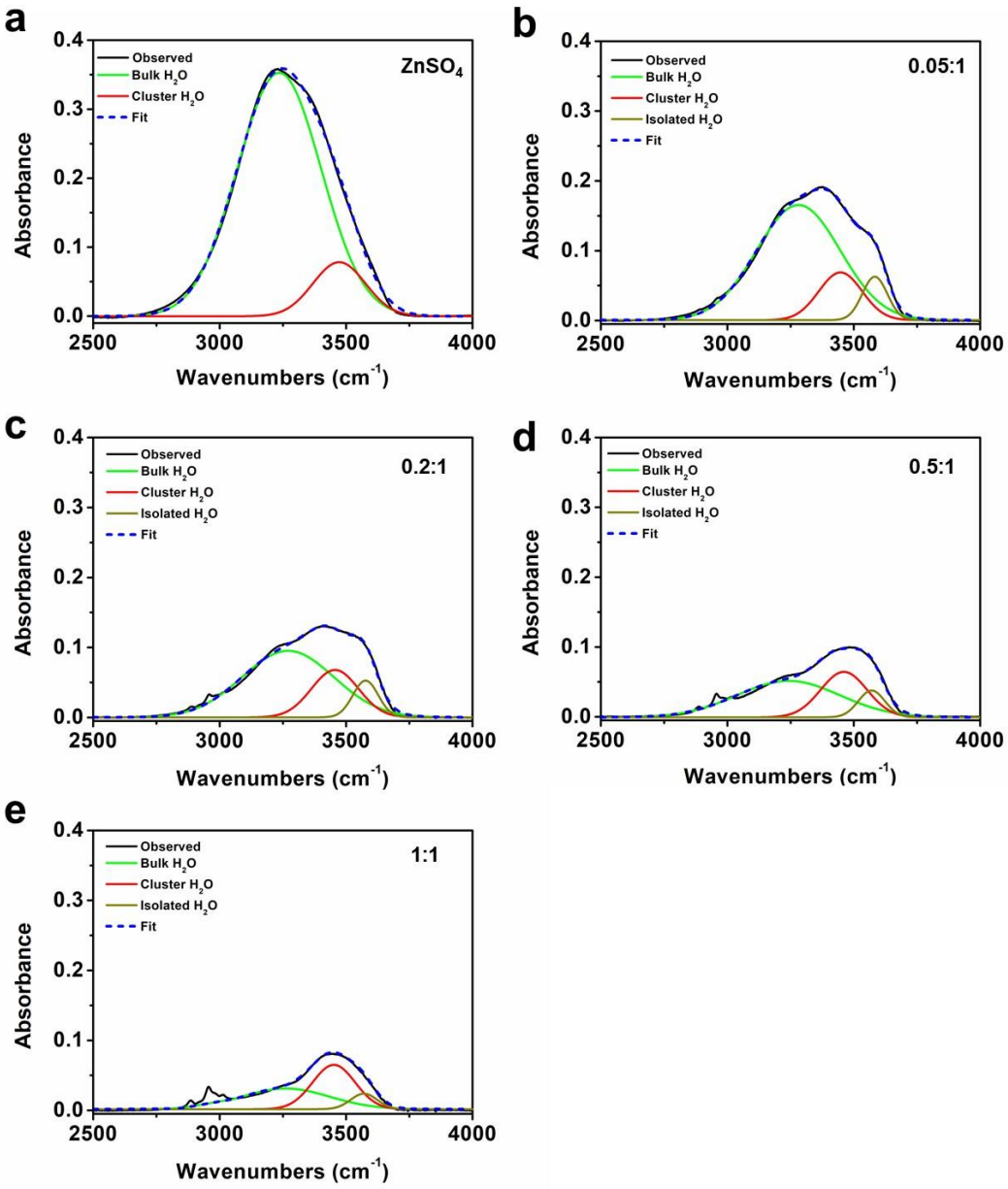

Figure S4. The fitted FTIR spectra of $ZnSO_4$, 0.05:1, 0.2:1, 0.5:1, and 1:1 sulfolane−H_2O hybrid $Zn(TFSI)_2$ electrolytes.

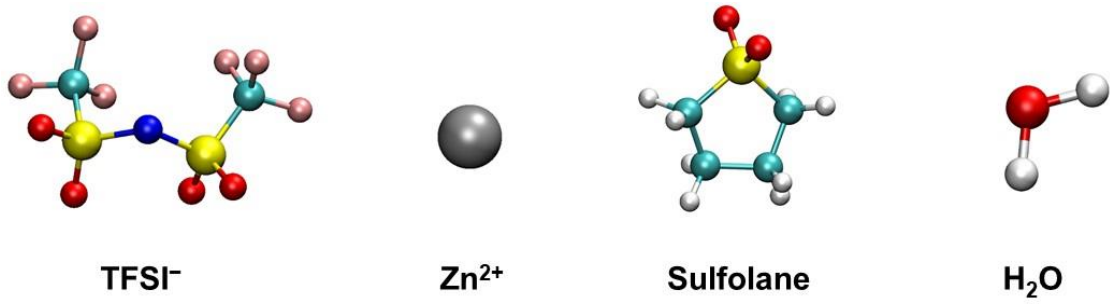

Figure S5. Schematic diagram of molecules or ions in MD calculations.

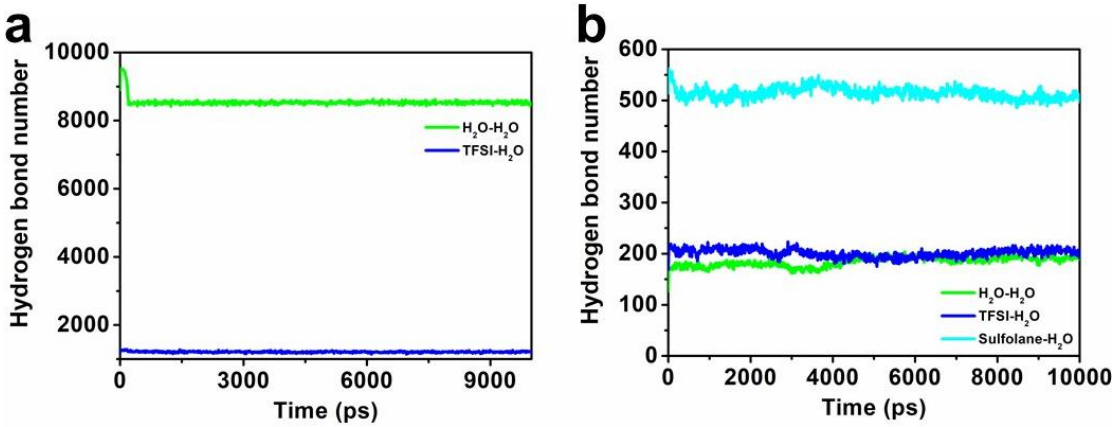

Figure S6. MD calculations number of different hydrogen bond type in (a) pure aqueous 1 M $Zn(TFSI)_2$ electrolyte and (b) sulfolane−H_2O hybrid electrolyte (2:1).

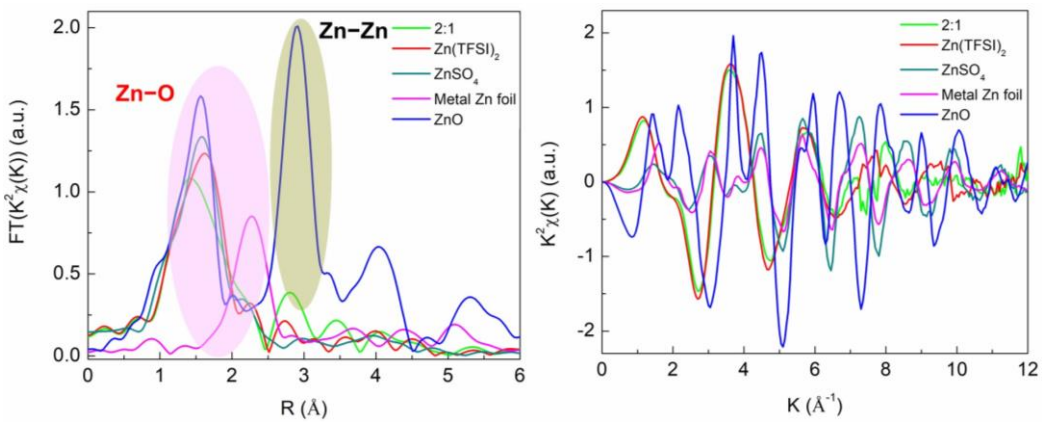

Figure S7. FT-EXAFS spectra at Zn K-edge at R space and K space.

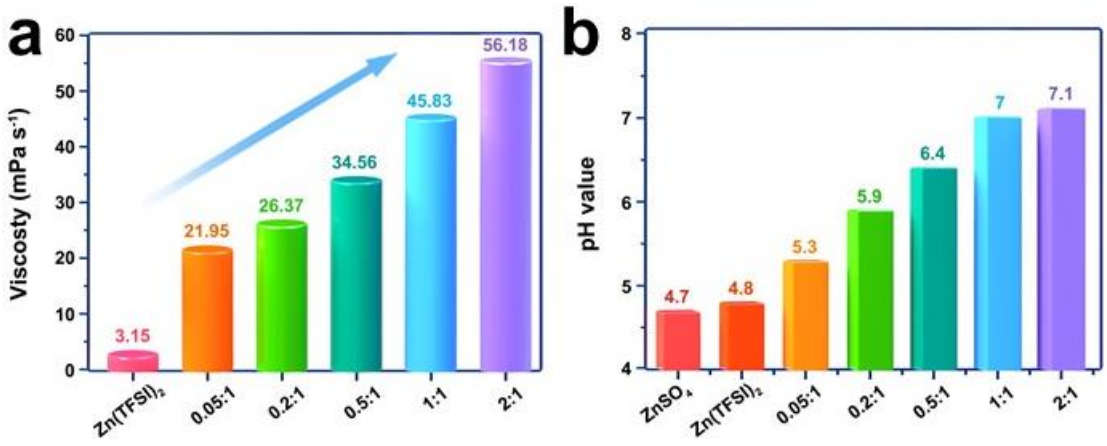

Figure S8. (a) Viscosity variation of sulfolane−H_2O hybrid electrolytes with different molar ratios. (b) pH value of different electrolytes.

Note: the pH of the electrolytes increases steadily with adding concentration of sulfolane from pH ≈ 4.8 in aqueous electrolytes (where the strong interaction of Zn^{2+} with H_2O leads to hydrolysis) to near pH ≈ 7, indicating that hydrolysis is effectively inhibited.

Figure S9. The Optical image of water evaporative properties test in different electrolytes and corresponding mass changes.

Note: The weight retention of different electrolytes is stark contrasting when exposed to an open atmosphere. For the sulfolane−H_2O hybrid electrolytes, not only retains water but there is a slight weight gain, indicating that the electrolyte actually extracts water from the environment. This unique property effectively eliminates concerns about water loss when used in open conditions, thus significantly improving the environmental suitability of aqueous electrolytes

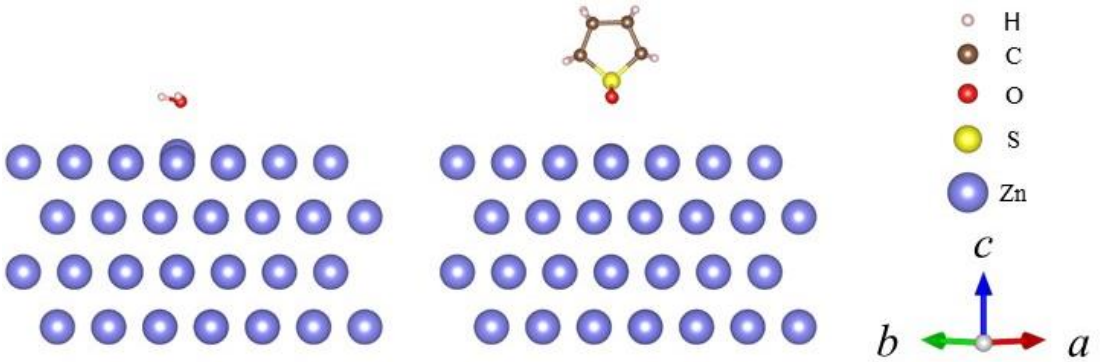

Figure S10. Schematic diagram of the model of sulfolane and water molecules in Zn(0001)

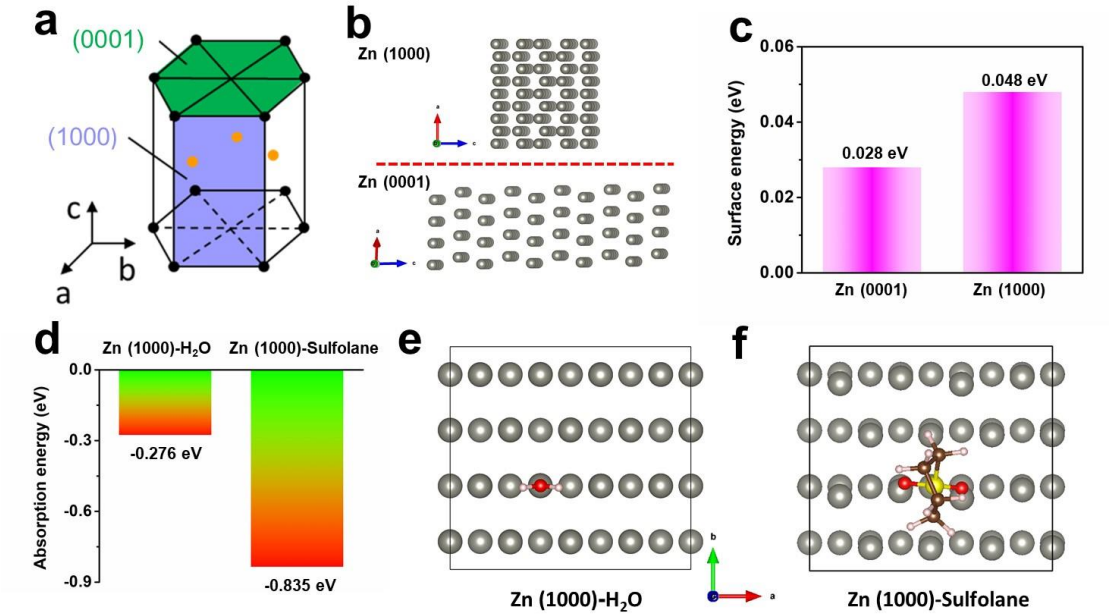

Figure S11. (a) The crystalline structure of metal Zn. (c) Comparing the surface energies of different crystal planes. (b) Schematic diagram of different crystal planes of Zn. (d) Adsorption energy comparison of H_2O and sulfolane molecule on Zn (1000) crystal plane and (e, f) schematic diagram of the model of sulfolane and water molecules in Zn(1000).

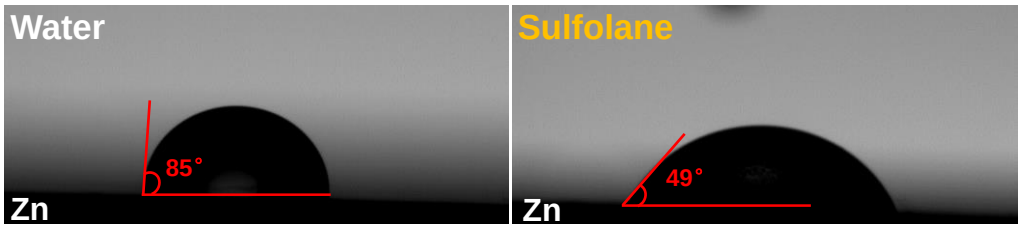

Figure S12. Wetting angles of water and sulfolane droplet on Zn foil.

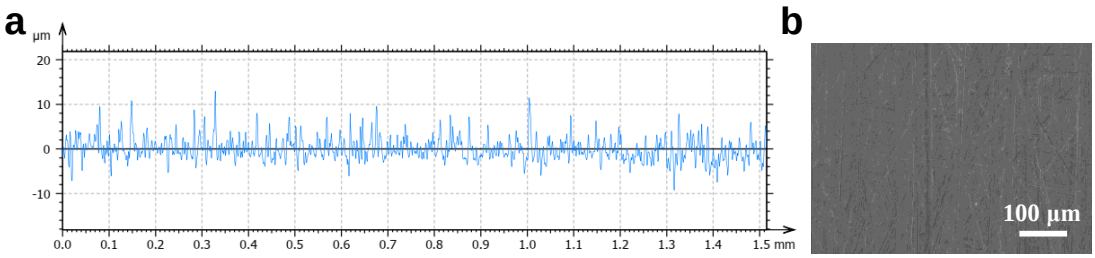

Figure S13. The surface roughness measurement of original Zn foil.

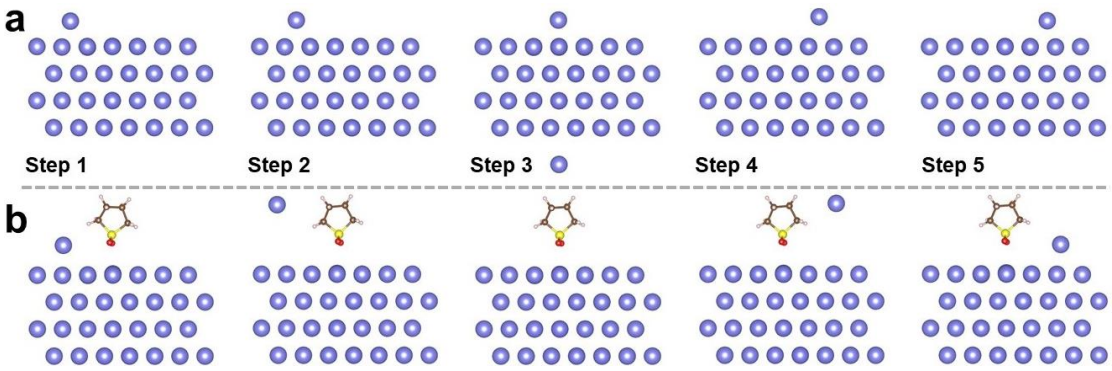

Figure S14. The corresponding schematic diagram of the migration site, (a) Zn migration on Zn (0001), (b) Zn migration on Zn (0001) with sulfolane.

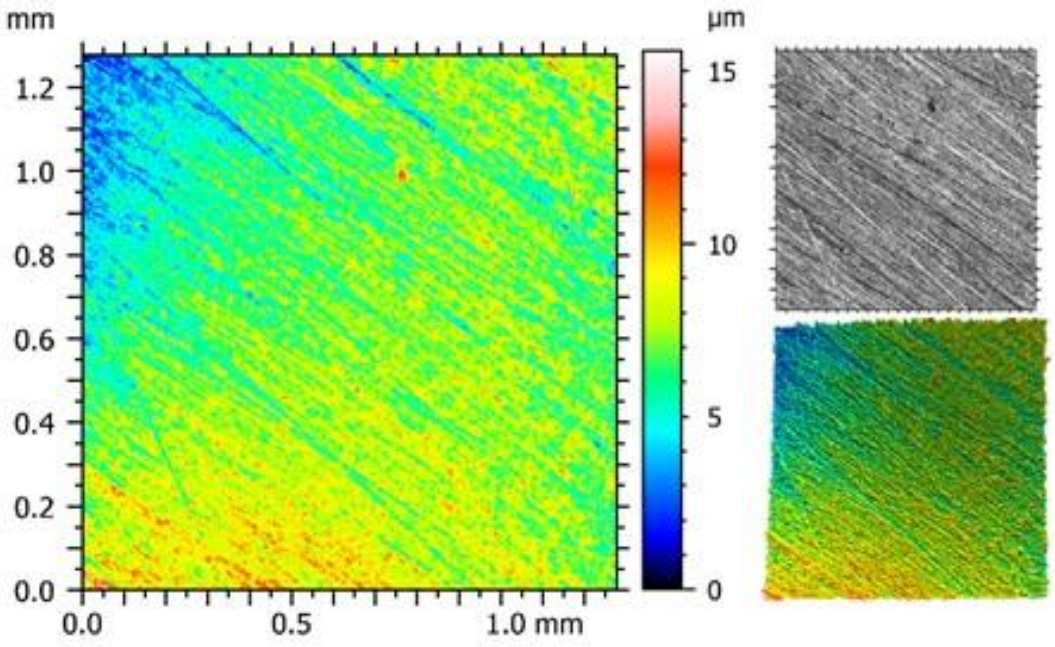

Figure S15. 3D height images for the original Zn anode surface.

Table S1. Comparison of the stability of this work with other reported works.

Zinc anode protection	Specific capacity/Current density	Cycle life
This work	**0.5 mAh cm^{-2}/0.5 mA cm^{-2}**	**8800h**
	1 mAh cm^{-2}/1 mA cm^{-2}	**9600h**
7.6 m $ZnCl_2$+0.05 m $SnCl_2$ electrolyte[12]	1 mAh cm^{-2}/1 mA cm^{-2}	500h
1m $ZnSO_4$+4 M EMImCl electrolyte[13]	1 mAh cm^{-2}/1 mA cm^{-2}	500h
3m $ZnSO_4$/H_2O/EG hybrid electrolyte[14]	0.5 mAh cm^{-2}/0.5 mA cm^{-2}	1334h
2m $ZnSO_4$+EG[15]	1 mAh cm^{-2}/2 mA cm^{-2}	145h
$Zn(TFSI)_2$-TFEP@MOF electrolyte[16]	0.5 mAh cm^{-2}/0.5 mA cm^{-2}	700h
0.5 m $Zn(CF_3SO_3)_2$-TEP electrolyte[17]	0.5 mAh cm^{-2}/0.5 mA cm^{-2}	3000h
acetamide-$Zn(TFSI)_2$ eutectic electrolyte[18]	0.5 mAh cm^{-2}/1 mA cm^{-2}	100h
4 M $Zn(BF_4)_2$ +2 mM $Al(OTf)_3$ electrolyte[19]	0.5 mAh cm^{-2}/1 mA cm^{-2}	1800h
$Zn(ClO_4)_2$·$6H_2O$ in succinonitrile electrolyte[20]	0.5 mAh cm^{-2}/0.05 mA cm^{-2}	800h
2m $Zn(BF_4)_2$ in [EMIM]BF_4 electrolyte[21]	1 mAh cm^{-2}/2 mA cm^{-2}	1500h
$ZnSO_4$+glucose electrolyte[22]	1 mAh cm^{-2}/1 mA cm^{-2}	2000h
ZnSO4+Arg electrolyte[23]	1 mAh cm^{-2}/1 mA cm^{-2}	2950h
$ZnCl_2$−H_2O−DMSO electrolyte[24]	0.5 mAh cm^{-2}/0.5 mA cm^{-2}	1000h
ZnGaIn//MXene[25]	1 mAh cm^{-2}/1 mA cm^{-2}	600h
Carbon hollow-spheres with zincophilic nitrogen sites[26]	1 mAh cm^{-2}/4 mA cm^{-2}	117h
ZnS@Zn-350[27]	2 mAh cm^{-2}/2 mA cm^{-2}	1100h
ZF@F-TiO_2[28]	1 mAh cm^{-2}/1 mA cm^{-2}	460h
Hydrogen-substituted graphdiyne@Zn[29]	1 mAh cm^{-2}/1 mA cm^{-2}	2400h
PVB@Zn[30]	0.5 mAh cm^{-2}/0.5 mA cm^{-2}	2200h
Zn@ZnO[31]	1.25 mAh cm^{-2}/5 mA cm^{-2}	500h
MOF-coated Zn anode[32]	0.5 mAh cm^{-2}/0.5 mA cm^{-2}	3000h
Texture Zn (002)[33]	0.5 mAh cm^{-2}/0.5 mA cm^{-2}	500h

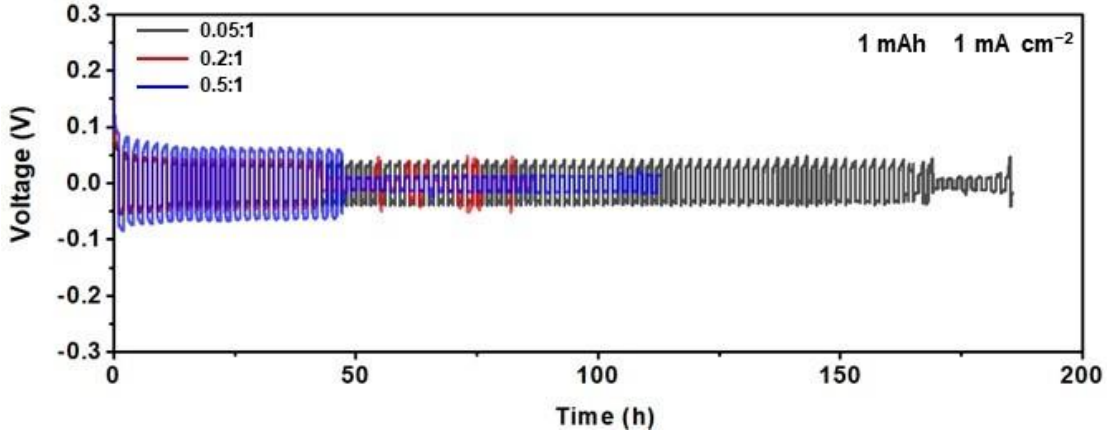

Figure S16. XRD results of Zn electrode after cycles in different electrolytes.

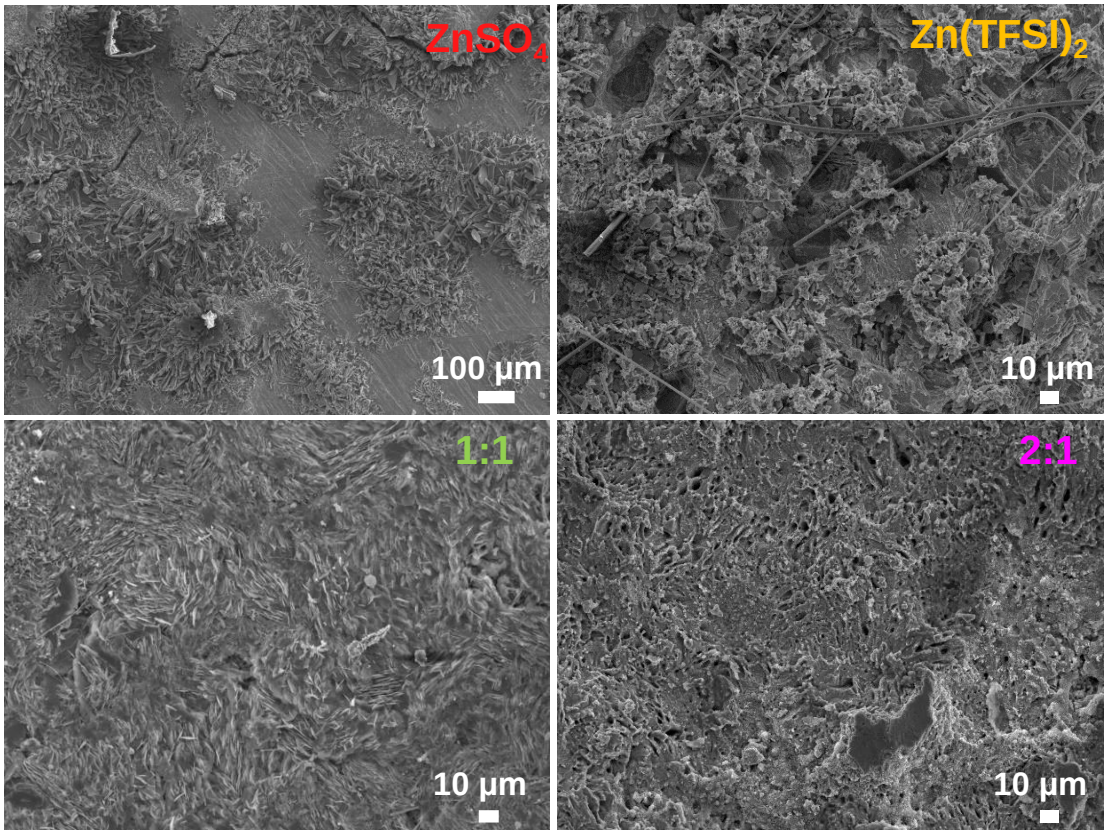

Figure S17. SEM images of Zn electrode after cycles in different electrolytes.

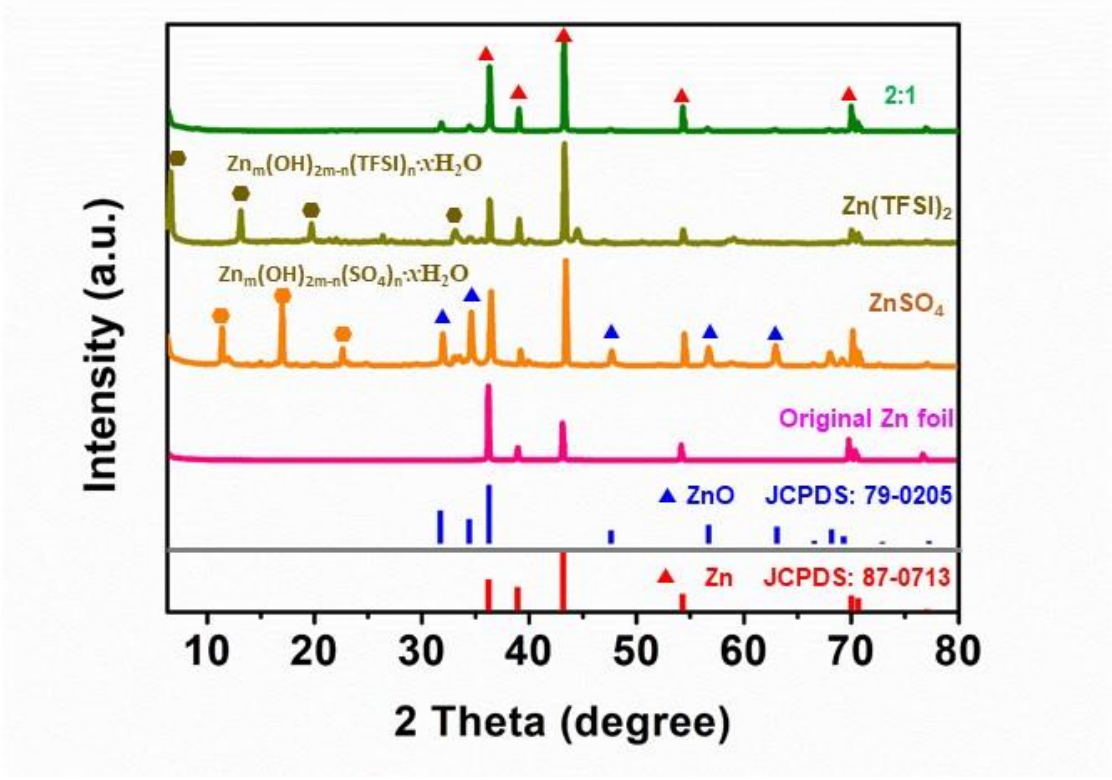

Figure S18. XRD results of Zn electrode after cycles in different electrolytes.

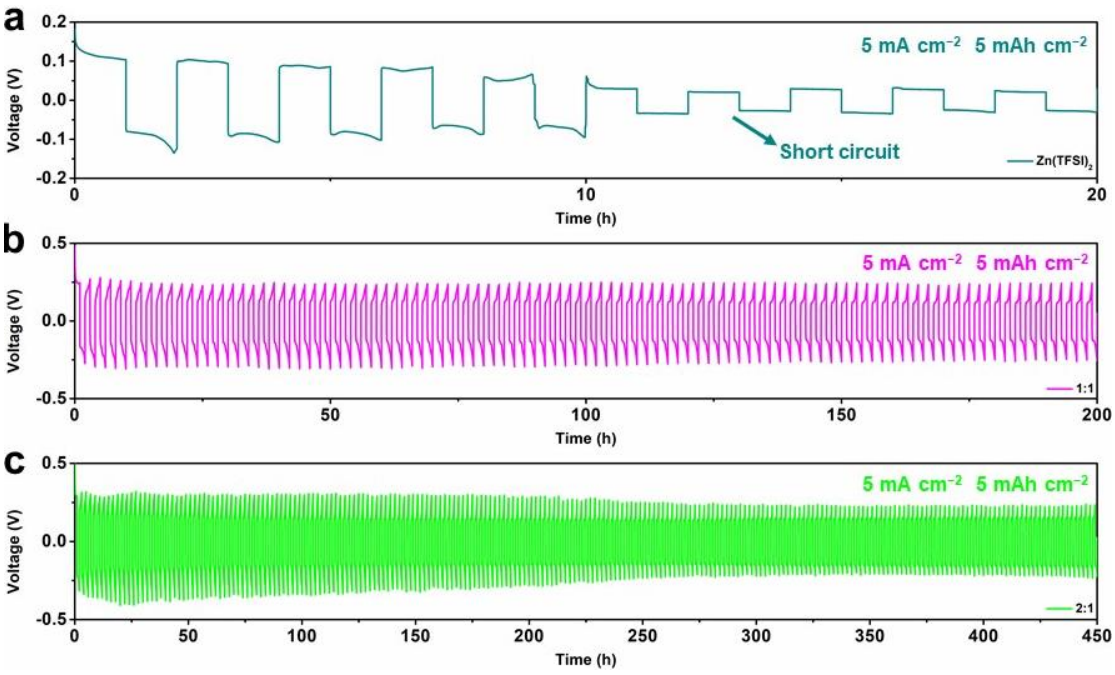

Figure S19. Galvanostatic Zn plating/stripping in Zn||Zn batteries in (a) $Zn(TFSI)_2$, (b) 1:1 and (c) 2:1 electrolytes at 5 mA cm^{-2} with 5 mA h cm^{-2}.

Note: For pure aqueous $Zn(TFSI)_2$ electrolyte, the short circuit appears after a short cycle of 10 h (Figure S17a). As a comparison, both 2:1 and 1:1 electrolytes demonstrate superior cycle stability (Figure S17b and c). In fact,

the sulfolane hybrid electrolyte all achieves the significant stability improvement at different currents and capacities, suggesting the high effectiveness of integrated electrolyte regulation strategies.

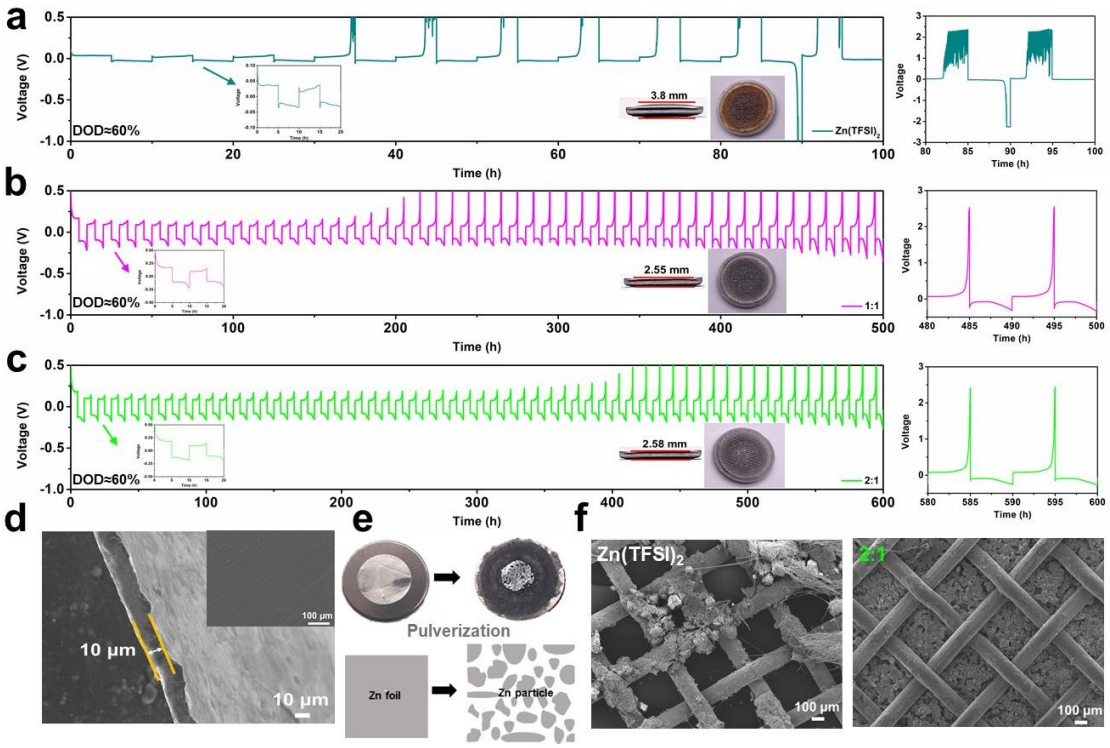

Figure S20. The Galvanostatic Zn plating/stripping in Zn||Zn cells in (a) $Zn(TFSI)_2$, (b) 1:1 and (c) 2:1 electrolytes at 60% DOD with 1 mA cm^{-2}/5 mA h cm^{-2}. The insets show the initial two cycles curve and the optical images of battery after cycling. (d) SEM images of original Zn foil. (e) Comparison of Zn foil before and after cycling at 60% DOD. (f) SEM images of Zn foil before and after cycling at 60%

DOD.

Note: At such high utilization rates, the plating/stripping of the Zn electrode is only stable for 30 h in pure aqueous $Zn(TFSI)_2$ electrolyte, after which significant polarization and battery failure occurs. Significant battery bulging can be found accompanied by severe corrosion due to the large amount of gas produced by severe water decomposition and pH changes (Figure S18a). For comparison, the sulfolane hybrid electrolyte exhibits

significantly improved plating/stripping stability. It is worth noting that despite the increased polarizations occurred after a long cycles, the plating/stripping is still stable and does not lead to bulging or corrosion of the cell due to water decomposition (Figure S18b and c). The polarizations occur due to the Zn plating in the stainless steel mesh (collector) as a result of the pulverization of the Zn foil at ultra-high DOD (Figure S18d-f). The process is similar to a Zn//Cu or Zn//Ti half-cell due to the significant increase in polarization caused by the deposition potential of the different metals. If we set the deposition cut-off voltage to 0.5V, similar to a Zn-Ti half-cell, the average high Coulombic efficiency can be achieved over 99%, demonstrating the significant enhanced stability both in electrolyte and Zn electrode.

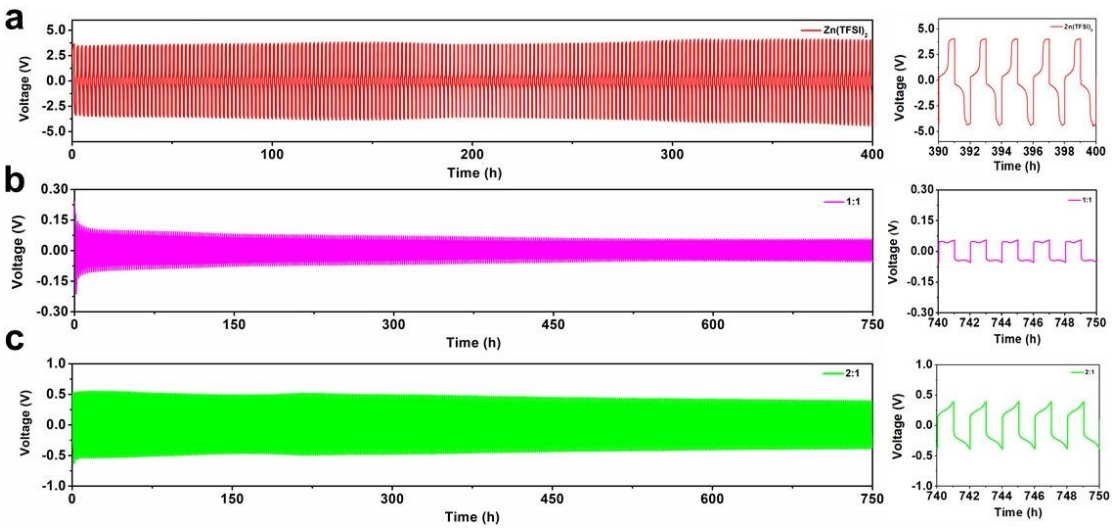

Figure S21. Galvanostatic cycling of symmetrical coin batteries in different electrolytes of (a) $Zn(TFSI)_2$, (b) 1:1, and (c) 2:1 at low temperature of −20 °C, with 0.5 mA cm^{-2} for 0.5 mAh cm^{-2}.

Note: Electroplating/stripping tests at a low temperature of −20 °C for Zn symmetric cells demonstrate the unparalleled frost resistance of the 1:1 and 2:1 hybrid electrolytes. The pure aqueous electrolyte $Zn(TFSI)_2$ electrolyte show the huge voltage polarization due to water freezing, suggesting a sluggish Zn^{2+} ion diffusion rate. There are no common problems such as short circuit during the whole cycle, which may be due to the fact that the iced electrolyte resembles the all-solid-state electrolyte, thus preventing the penetration of dendrites causing short circuits.

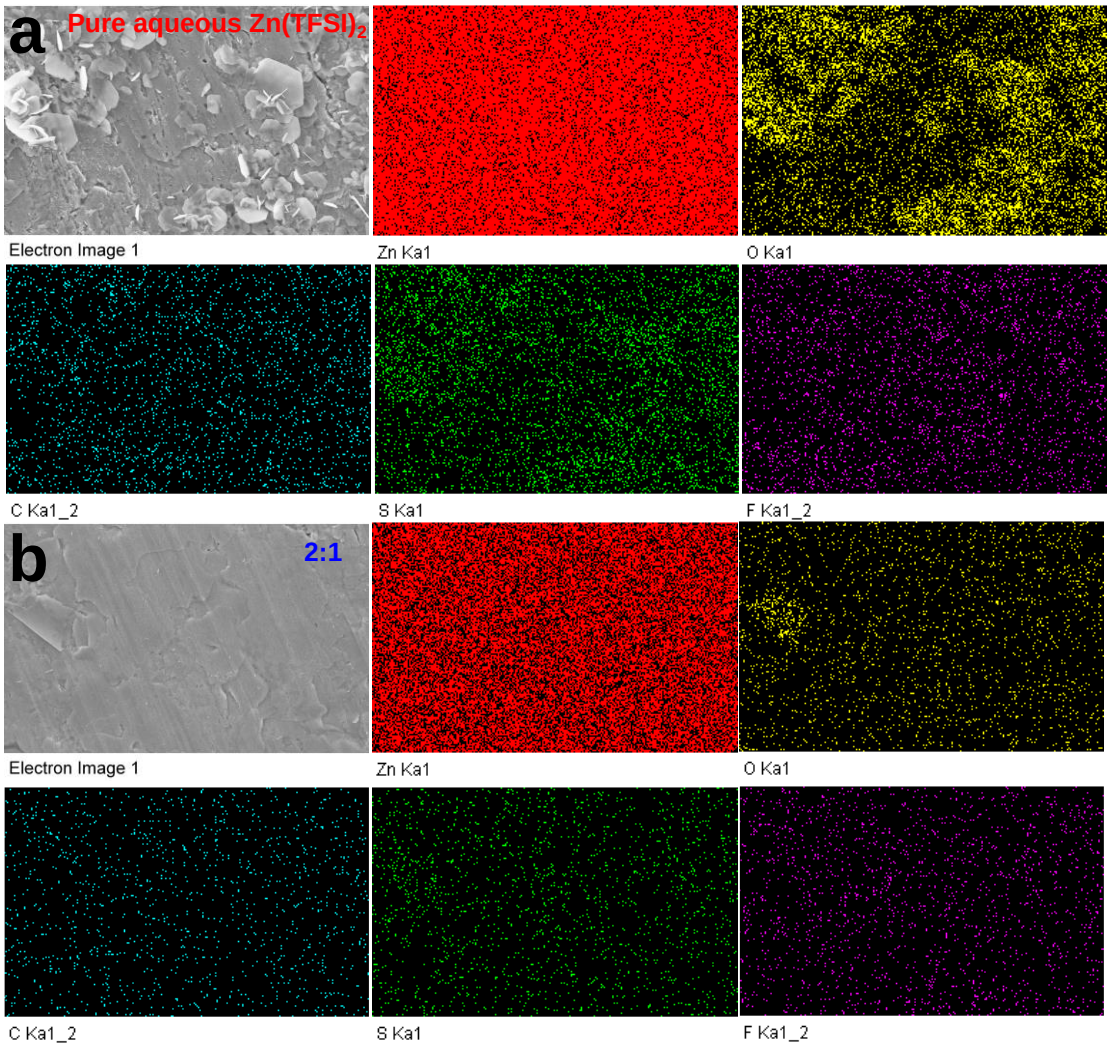

Figure S22. The SEM images and corresponding element mappings of Zn foil after soaking in (a) pure aqueous $Zn(TFSI)_2$ and 2:1 electrolyte for one week.

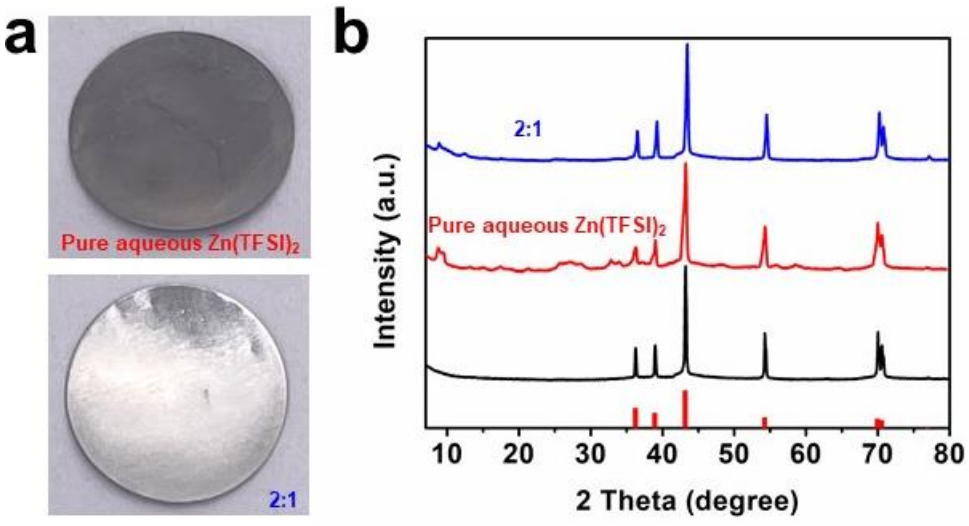

Figure S23. (a) Optical photos of Zn anode after immersion in different electrolytes of pure aqueous $Zn(TFSI)_2$

(top) electrolyte and 2:1 (bottom). (b) XRD results after soaking.

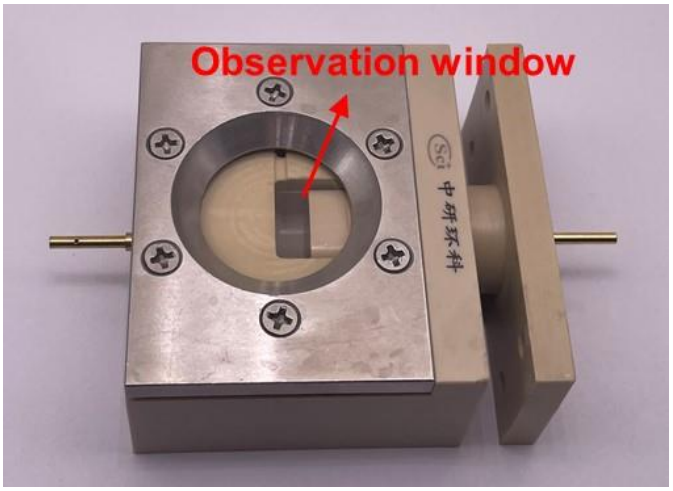

Figure S24. Optical cells for in-situ observation of the Zn plating process.

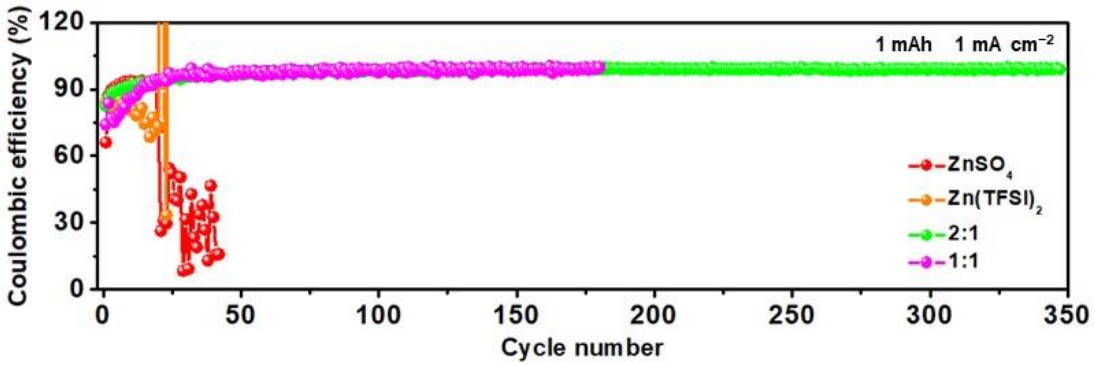

Figure S25. Coulombic efficiency of Zn//Ti batteries in different electrolytes.

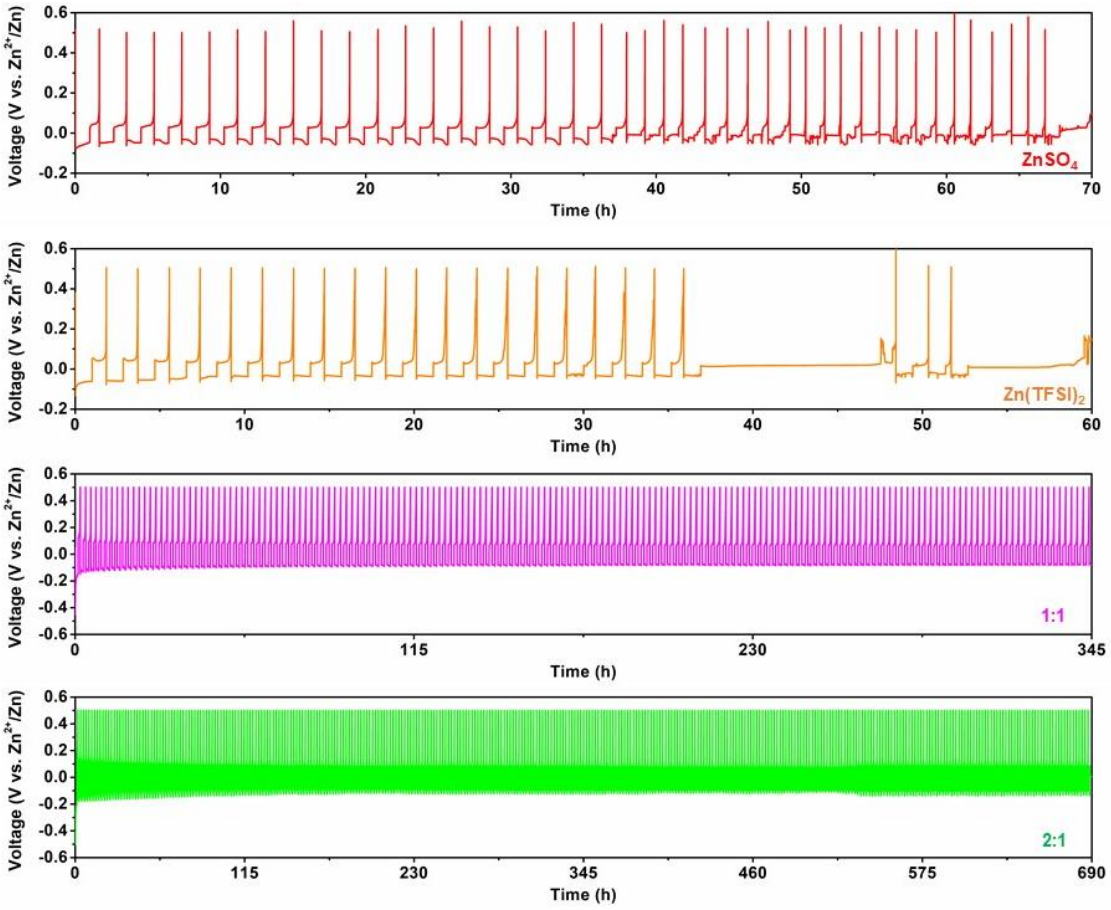

Figure S26. Galvanostatic charge−discharge curves of Zn//Ti batteries in different electrolytes under 1 mA cm^{-2}/1 mAh cm^{-2}.

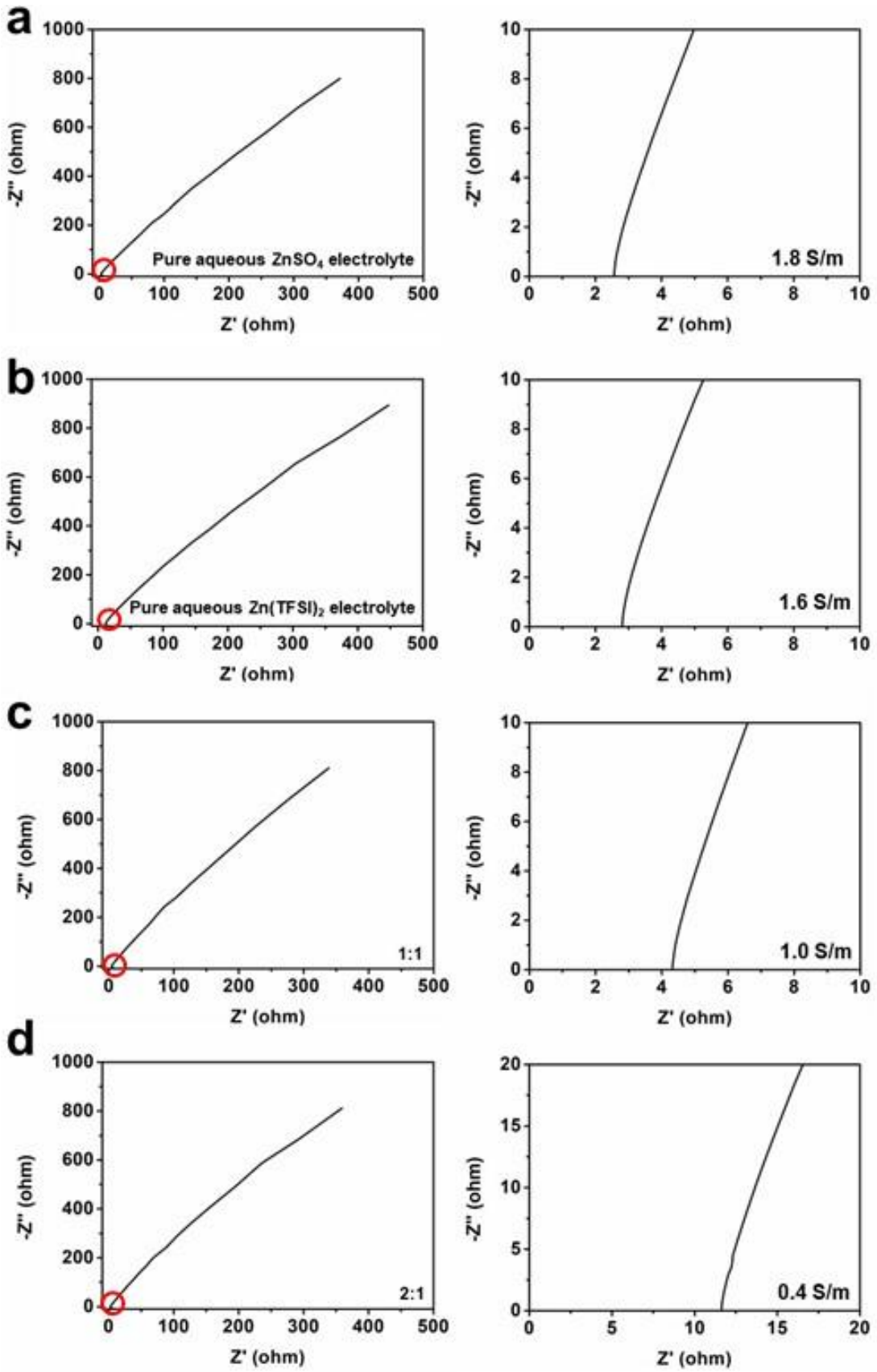

Figure S27. The A. C. impedance spectra of symmetric cells assembled by pure aqueous electrolytes of (a) $ZnSO_4$, (b) $Zn(TFSI)_2$, and hybrid electrolytes of (c) 1:1, (d) 2:1.

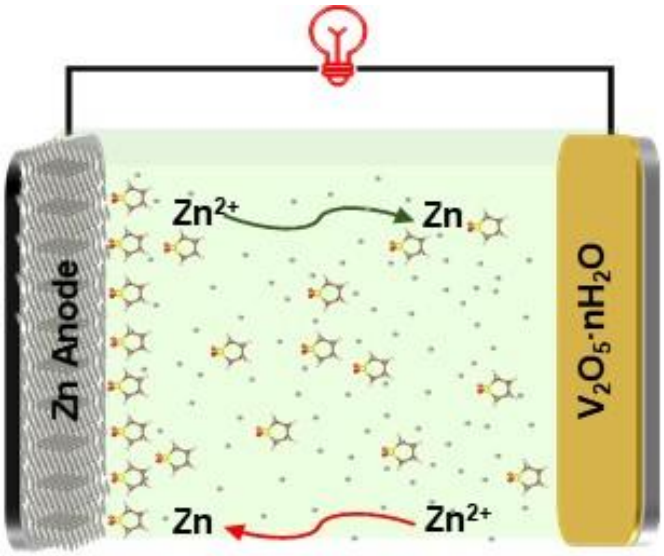

Figure S28. Schematic diagram for the Zn-ion full battery enabled by Zn foil as anode, VOH as cathode, 1M $Zn(TFSI)_2$ as sulfolane−H_2O hybrid electrolytes.

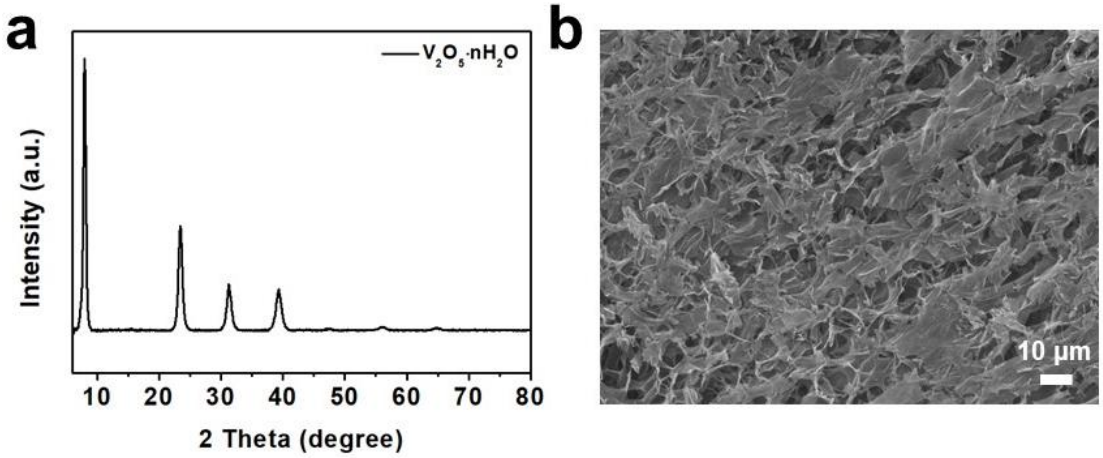

Figure S29. (a) The XRD result and (b) SEM image of $V_2O_5 \cdot nH_2O$.

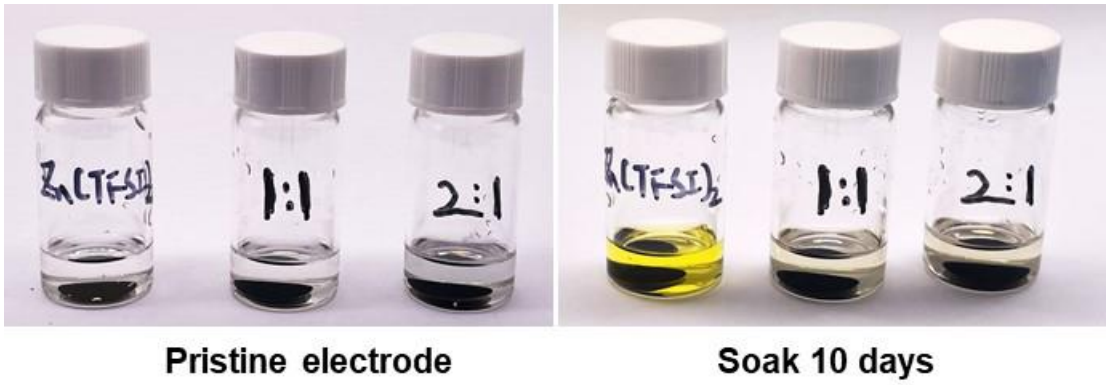

Figure S30. The optical images of VOH electrodes after immersion in different electrolytes for ten days.

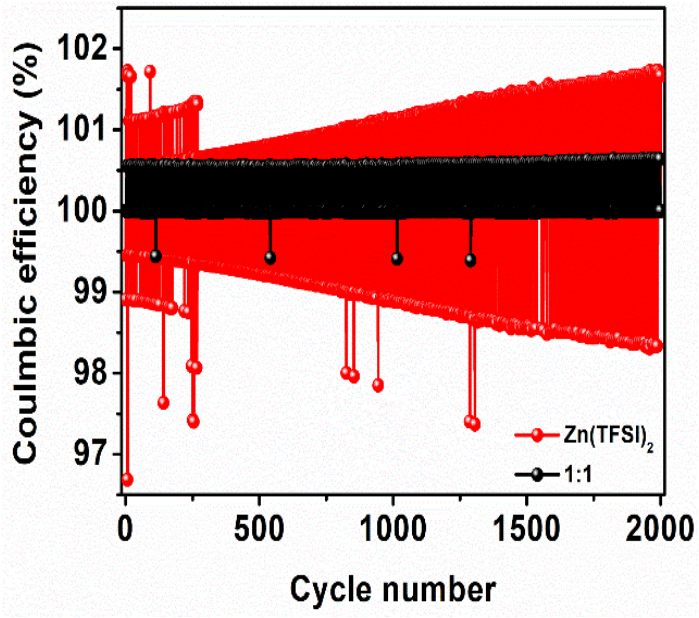

Figure S31. The coulombic efficiency of Zn//VOH batteries during cycles with different electrolytes.

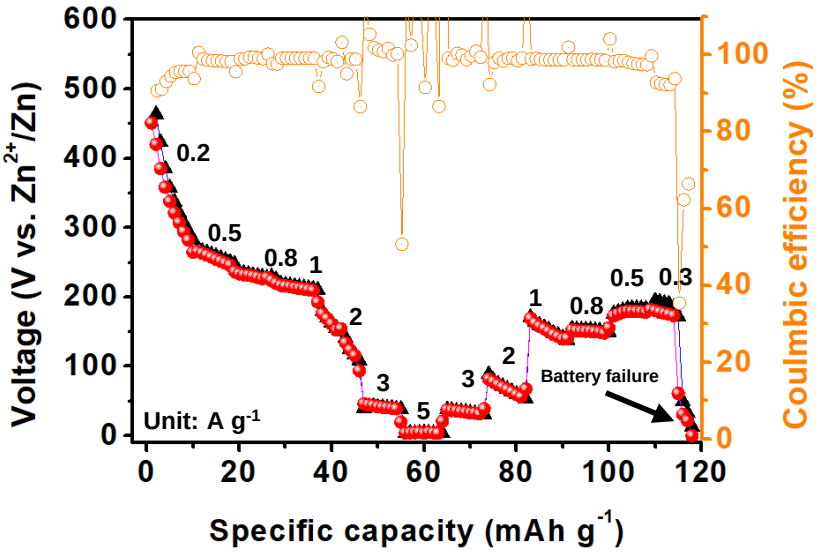

Figure S32. Rate performances of Zn-VOH batteries based on pure aqueous Zn(TFSI)2 electrolyte at low temperature of −20 ℃.

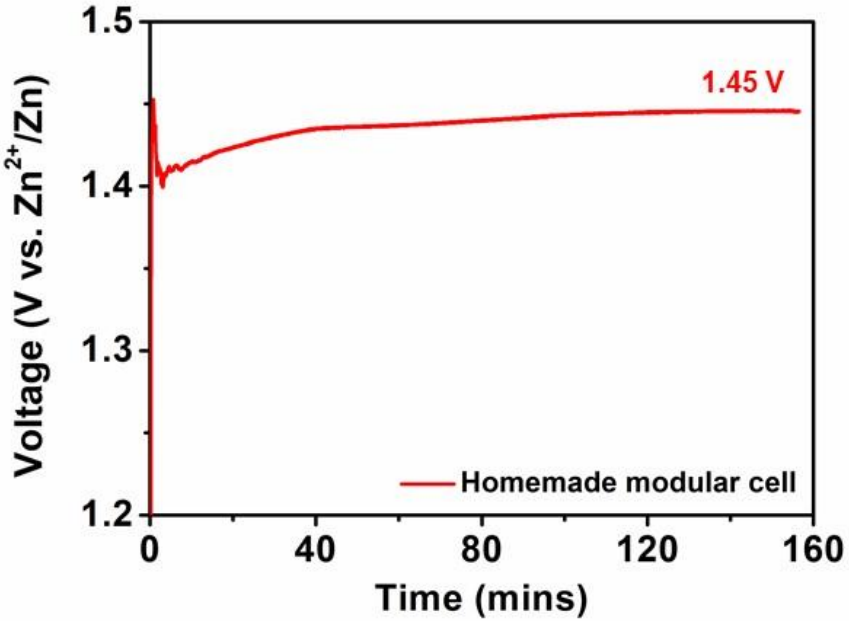

Figure S33. The voltage resting curve of the homemade modular cell.

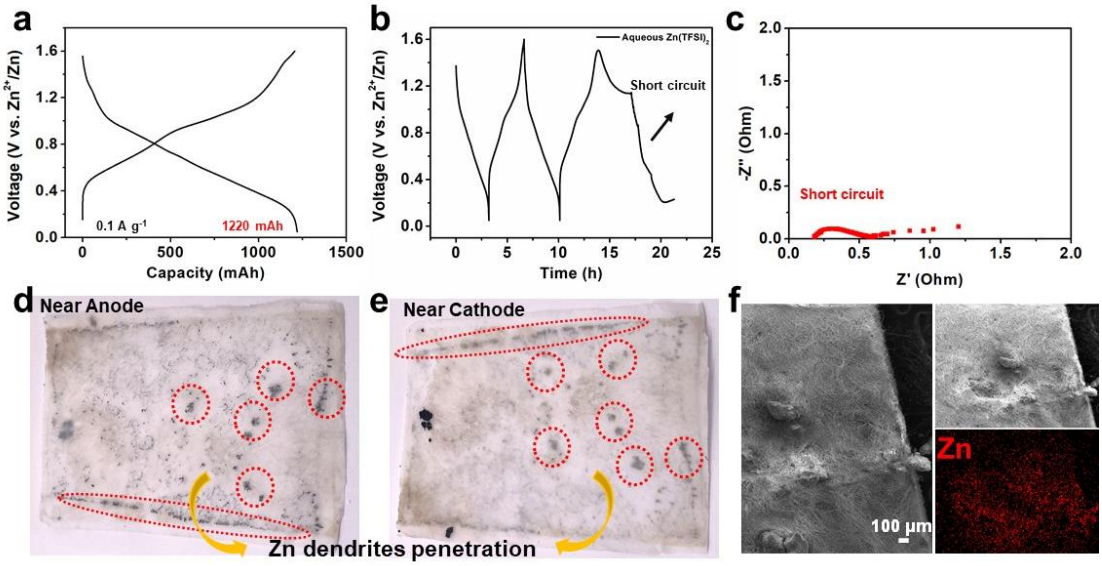

Figure S34. (a, b) Galvanostatic discharge−charge voltage profiles of Zn//VOH pouch cell at a current density of 0.1 A g^{-1}. (c) EIS result of Zn//VOH pouch cell after short circuit. (d, e) The optical images of separator, (f) SEM and corresponding mapping image.

Figure S35. The optical images of Zn anode and separator of Zn//VOH pouch cell based 1:1 hybrid electrolyte after cycles.

Table S2. Parameters of the Zn//VOH pouch cell at the Ah level.

	Parameter	Value
VOH cathode	Discharge capacity	330mAh g^{-1} at 0.1A g^{-1}
	Active material ration	VOH : Super P : PTFE= 7 : 2 : 1
	Mass loading	15 mg cm^{-1}
	Number of stacks	6
	Electrode area	5 cm * 9 cm =45 cm^{-2}
	Area capacity	4.89 mAh cm^{-2}
	Electrode thickness	0.2 mm
	VOH power amount	4000 mg (50 mg loss)
Separator	Thickness	160 μm, glass fiber
	Number of stacks	11
Zn foil anode	Thickness	100 μm
	Theoretical capacity	820 mAh g^{-1}
	Number of stacks	6
Electrolytes	Volume	10 mL Ah^{-1}
Package	Aluminium plastic film	80 μm
Cell	Capacity	1.32 Ah
	Energy	948.8 mWh
	Cell energy based on the mass VOH and theoretically used Zn	206.3 Wh kg^{-1}
	Cell energy based on volume	59.3 Wh L^{-1}

Reference:

[1] Y. Yang, Y. Tang, G. Fang, L. Shan, J. Guo, W. Zhang, C. Wang, L. Wang, J. Zhou, S. Liang, *Energy. Environ. Sci.* **2018**, 11, 3157.

[2] M. J. Abraham, T. Murtola, R. Schulz, S. Páll, J. C. Smith, B. Hess, E. Lindahl, *SoftwareX* **2015**, 1-2, 19.

[3] L. Martinez, R. Andrade, E. G. Birgin, J. M. Martinez, *J. Comput. Chem.* **2009**, 30, 2157.

[4] J. Wang, R. M. Wolf, J. W. Caldwell, P. A. Kollman, D. A. Case, *J. Comput. Chem.* **2004**, 25, 1157.

[5] H. J. C. Berendsen, J. R. Grigera, T. P. Straatsma, *J. Phys. Chem.* **1987**, 91, 6269.

[6] P. Li, B. P. Roberts, D. K. Chakravorty, K. M. Merz, Jr., *J. Chem. Theory Comput.* **2013**, 9, 2733.

[7] T. Lu, F. Chen, *J. Comput. Chem.* **2012**, 33, 580.

[8] a) G. Kresse, J. Hafner, *Phys. Rev. B* **1994**, 49, 14251; b) G. Kresse, J. Furthmüller, *Comput. Mater. Sci.* **1996**, 6.

[9] a) P. E. Blochl, O. Jepsen, O. K. Andersen, *Phys. Rev. B* **1994**, 49, 16223; b) G. Kresse, D. Joubert, *Phys. Rev. B* **1999**, 59, 1758; c) J. P. Perdew, K. Burke, M. Ernzerhof, *Phys. Rev. Lett.* **1996**, 77 3865.

[10] a) L. Kabalan, I. Kowalec, C. R. A. Catlow, A. J. Logsdail, *Phys. Chem. Chem. Phys.* **2021**, 23, 14649; b) R. Tran, Z. Xu, B. Radhakrishnan, D. Winston, W. Sun, K. A. Persson, S. P. Ong, *Sci. Data* **2016**, 3, 160080.

[11] a) G. Henkelman, B. P. Uberuaga, H. Jónsson, *J. Chem. Phys.* **2000**, 113, 9901; b) G. Henkelman, H. Jónsson, *J. Chem. Phys.* **2000**, 113, 9978.

[12] L. Cao, D. Li, F. A. Soto, V. Ponce, B. Zhang, L. Ma, T. Deng, J. M. Seminario, E. Hu, X. Q. Yang, P. B. Balbuena, C. Wang, *Angew. Chem. Int. Ed.* **2021**, 60, 18845.

[13] Q. Zhang, Y. Ma, Y. Lu, X. Zhou, L. Lin, L. Li, Z. Yan, Q. Zhao, K. Zhang, J. Chen, *Angew. Chem. Int. Ed.* **2021**, 60, 23357.

[14] R. Qin, Y. Wang, M. Zhang, Y. Wang, S. Ding, A. Song, H. Yi, L. Yang, Y. Song, Y. Cui, J. Liu, Z. Wang, S. Li, Q. Zhao, F. Pan, *Nano Energy* **2021**, 80, 105478.

[15] N. Chang, T. Li, R. Li, S. Wang, Y. Yin, H. Zhang, X. Li, *Energy Environ. Sci.* **2020**, 13, 3527.

[16] L. Cao, D. Li, T. Deng, Q. Li, C. Wang, *Angew. Chem. Int. Ed.* **2020**, 59, 19292.

[17] A. Naveed, H. Yang, J. Yang, Y. Nuli, J. Wang, *Angew. Chem. Int. Ed.* **2019**, 58, 2760.

[18] H. Qiu, X. Du, J. Zhao, Y. Wang, J. Ju, Z. Chen, Z. Hu, D. Yan, X. Zhou, G. Cui, *Nat. Commun.* **2019**, 10, 5374.

[19] L. Ma, S. Chen, X. Li, A. Chen, B. Dong, C. Zhi, *Angew. Chem. Int. Ed.* **2020**, 59, 23836.

[20] W. Yang, X. Du, J. Zhao, Z. Chen, J. Li, J. Xie, Y. Zhang, Z. Cui, Q. Kong, Z. Zhao, C. Wang, Q. Zhang, G. Cui, *Joule* **2020**, 4, 1557.

[21] L. Ma, S. Chen, N. Li, Z. Liu, Z. Tang, J. A. Zapien, S. Chen, J. Fan, C. Zhi, *Adv. Mater.* **2020**, 32, e1908121.

[22] P. Sun, L. Ma, W. Zhou, M. Qiu, Z. Wang, D. Chao, W. Mai, *Angew. Chem. Int. Ed.* **2021**, 60, 18247.

[23] H. Lu, X. Zhang, M. Luo, K. Cao, Y. Lu, B. B. Xu, H. Pan, K. Tao, Y. Jiang, *Adv. Funct. Mater.* **2021**, 31, 2103514.

[24] L. Cao, D. Li, E. Hu, J. Xu, T. Deng, L. Ma, Y. Wang, X. Q. Yang, C. Wang, *J. Am.*

Chem. Soc. **2020**, 142, 21404.

[25] J. Gu, Y. Tao, H. Chen, Z. Cao, Y. Zhang, Z. Du, Y. Cui, S. Yang, *Advanced Energy Materials* n/a, 2200115.

[26] F. Xie, H. Li, X. Wang, X. Zhi, D. Chao, K. Davey, S. Z. Qiao, *Adv. Energy Mater.* **2021**, 11, 2003419.

[27] J. Hao, B. Li, X. Li, X. Zeng, S. Zhang, F. Yang, S. Liu, D. Li, C. Wu, Z. Guo, *Adv. Mater.* **2020**, 32, e2003021.

[28] Q. Zhang, J. Luan, X. Huang, Q. Wang, D. Sun, Y. Tang, X. Ji, H. Wang, *Nat. Commun.* **2020**, 11, 3961.

[29] Q. Yang, Y. Guo, B. Yan, C. Wang, Z. Liu, Z. Huang, Y. Wang, Y. Li, H. Li, L. Song, J. Fan, C. Zhi, *Adv. Mater.* **2020**, 32, e2001755.

[30] J. Hao, X. Li, S. Zhang, F. Yang, X. Zeng, S. Zhang, G. Bo, C. Wang, Z. Guo, *Adv. Funct. Mater.* **2020**, 30, 2001263.

[31] X. Xie, S. Liang, J. Gao, S. Guo, J. Guo, C. Wang, G. Xu, X. Wu, G. Chen, J. Zhou, *Energy Environ. Sci.* **2020**, 13, 503.

[32] H. Yang, Z. Chang, Y. Qiao, H. Deng, X. Mu, P. He, H. Zhou, *Angew. Chem. Int. Ed.* **2020**, 59, 9377.

[33] M. Zhou, S. Guo, J. Li, X. Luo, Z. Liu, T. Zhang, X. Cao, M. Long, B. Lu, A. Pan, G. Fang, J. Zhou, S. Liang, *Adv. Mater.* **2021**, 33, e2100187.